

Radiation dose reduction in medical x-ray CT via Fourier-based iterative reconstruction

Benjamin P. Fahimian

Department of Radiation Oncology, Stanford University, Stanford, California 94305

Yunzhe Zhao, Zhifeng Huang, and Russell Fung

Department of Physics and Astronomy and California NanoSystems Institute, University of California, Los Angeles, California 90095

Yu Mao

Institute for Mathematics and Its Applications, University of Minnesota, Minneapolis, Minnesota 55455

Chun Zhu

Department of Physics and Astronomy and California NanoSystems Institute, University of California, Los Angeles, California 90095

Maryam Khatonabadi and John J. DeMarco

Biomedical Physics Interdepartmental Program, David Geffen School of Medicine at UCLA, Los Angeles, California 90095-1770

Stanley J. Osher

Department of Mathematics, University of California, Los Angeles, California 90095

Michael F. McNitt-Gray

Biomedical Physics Interdepartmental Program, David Geffen School of Medicine at UCLA, Los Angeles, California 90095-1770

Jianwei Miao^{a)}

Department of Physics and Astronomy and California NanoSystems Institute, University of California, Los Angeles, California 90095

(Received 8 May 2012; revised 22 January 2013; accepted for publication 26 January 2013; published 28 February 2013)

Purpose: A Fourier-based iterative reconstruction technique, termed Equally Sloped Tomography (EST), is developed in conjunction with advanced mathematical regularization to investigate radiation dose reduction in x-ray CT. The method is experimentally implemented on fan-beam CT and evaluated as a function of imaging dose on a series of image quality phantoms and anonymous pediatric patient data sets. Numerical simulation experiments are also performed to explore the extension of EST to helical cone-beam geometry.

Methods: EST is a Fourier based iterative algorithm, which iterates back and forth between real and Fourier space utilizing the algebraically exact pseudopolar fast Fourier transform (PPFFT). In each iteration, physical constraints and mathematical regularization are applied in real space, while the measured data are enforced in Fourier space. The algorithm is automatically terminated when a proposed termination criterion is met. Experimentally, fan-beam projections were acquired by the Siemens z-flying focal spot technology, and subsequently interleaved and rebinned to a pseudopolar grid. Image quality phantoms were scanned at systematically varied mAs settings, reconstructed by EST and conventional reconstruction methods such as filtered back projection (FBP), and quantified using metrics including resolution, signal-to-noise ratios (SNRs), and contrast-to-noise ratios (CNRs). Pediatric data sets were reconstructed at their original acquisition settings and additionally simulated to lower dose settings for comparison and evaluation of the potential for radiation dose reduction. Numerical experiments were conducted to quantify EST and other iterative methods in terms of image quality and computation time. The extension of EST to helical cone-beam CT was implemented by using the advanced single-slice rebinning (ASSR) method.

Results: Based on the phantom and pediatric patient fan-beam CT data, it is demonstrated that EST reconstructions with the lowest scanner flux setting of 39 mAs produce comparable image quality, resolution, and contrast relative to FBP with the 140 mAs flux setting. Compared to the algebraic reconstruction technique and the expectation maximization statistical reconstruction algorithm, a significant reduction in computation time is achieved with EST. Finally, numerical experiments on

helical cone-beam CT data suggest that the combination of EST and ASSR produces reconstructions with higher image quality and lower noise than the Feldkamp Davis and Kress (FDK) method and the conventional ASSR approach.

Conclusions: A Fourier-based iterative method has been applied to the reconstruction of fan-beam CT data with reduced x-ray fluence. This method incorporates advantageous features in both real and Fourier space iterative schemes: using a fast and algebraically exact method to calculate forward projection, enforcing the measured data in Fourier space, and applying physical constraints and flexible regularization in real space. Our results suggest that EST can be utilized for radiation dose reduction in x-ray CT via the readily implementable technique of lowering mAs settings. Numerical experiments further indicate that EST requires less computation time than several other iterative algorithms and can, in principle, be extended to helical cone-beam geometry in combination with the ASSR method. © 2013 American Association of Physicists in Medicine. [<http://dx.doi.org/10.1118/1.4791644>]

Key words: Equally Sloped Tomography (EST), medical x-ray CT, radiation dose reduction, iterative algorithm, pseudopolar fast Fourier transform (PPFFT)

I. INTRODUCTION

Since its inception in the 1970s, x-ray computed tomography (CT) has become a revolutionary medical tool in the diagnosis of diseases and visualization of interventional procedures.¹⁻⁴ However, due to the tomographic acquisition requirement of sufficiently high flux projections from a multitude of directions, a major concern in medical CT is the resulting radiation dose delivered to the patient, especially to the more radiosensitive population such as pediatrics.⁵⁻⁹ According to the 2009 report from the National Council on Radiation Protection and Measurements,¹⁰ CT accounts for about 15% of the total radiological examinations, but is disproportionately responsible for approximately 50% of the medical radiation exposure and nearly 25% of the total population exposure. Recently, the combination of real space iterative algorithms with modern optimization methods has been investigated for radiation dose reduction in CT.¹¹⁻¹⁷ Although these methods perform well under certain circumstances, currently the most popular method in clinical CT and other tomographic fields remains filtered back projection (FBP) and its variations.^{18,19}

In 2005, a Fourier-based iterative method, denoted Equally Sloped Tomography (EST), was developed to allow the 3D image reconstruction from a limited number of projections in parallel beam geometry.²⁰ It has been shown that EST is an effective method for significant reduction of radiation dose in several tomographic applications, including transmission electron tomography, x-ray diffraction microscopy, and synchrotron based x-ray phase contrast and transmission CT.²⁰⁻²⁵ More recently, it has been demonstrated that EST can be used for 3D structure determination of nanomaterials at atomic scale resolution²⁶ as well as for high resolution, low dose phase contrast x-ray imaging of human breast cancers in three dimensions.²⁷ In this paper, we report the feasibility of using EST to reduce radiation dose in medical CT. We first present experimental results on the low-dose EST reconstructions of phantom and pediatric data sets in fan-beam geometry. We then demonstrate with numerical experiments that, in combination with the ASSR method, EST can in principle be extended to helical cone-beam geometry.

II. METHODS

II.A. The pseudopolar fast Fourier transform

In 2D parallel beam geometry, conventional equally angled acquisitions result in a polar distribution of measured data in Fourier space, while the transformed reconstructed images must be represented on a Cartesian grid. Although it is believed that no direct and exact FFT algorithm can be constructed between the polar and Cartesian grids,²⁸⁻³⁰ the existence of an algebraically exact FFT algorithm between the pseudopolar and Cartesian grids, denoted the PPFFT, has been demonstrated.^{31,32} As depicted in Fig. 1(a), for a $N \times N$ Cartesian grid, the pseudopolar grid is defined by a set of $2N$ lines, each line consisting of $2N$ grid points mapped out on N concentric squares. The $2N$ lines are subdivided into two groups: a horizontal group (in gray) and a vertical group (in red). These pseudopolar lines are termed “equally sloped” since the successive lines in both groups change by an equal sloped increment, as opposed to a fixed equal angled increment as in the polar grid. Unlike the polar grid, the distance between sampling points on the individual lines of the pseudopolar grid varies from line to line. The fractional Fourier transform (FrFT) can be used to vary the output sampling distance of the Fourier transform.³³ The 1D FrFT is defined by

$$F_a(k) = \sum_{x=0}^{N-1} f(x) \exp\left(-\frac{i2\pi\alpha kx}{N}\right). \quad (1)$$

It is noted that the pseudopolar grid and the PPFFT algorithm were originally developed to interpolate tomographic projections from the polar to the Cartesian grid in reciprocal space.^{31,32} The idea of acquiring tilt-series at equal slope increments and then combining the PPFFT with iterative algorithms for tomographic reconstructions was first proposed by Miao *et al.* in 2005.²⁰

II.B. The EST method

Although the PPFFT and its inverse provide an algebraically exact way to do the FFT between the Cartesian and pseudopolar grids, three difficulties limit its direct application

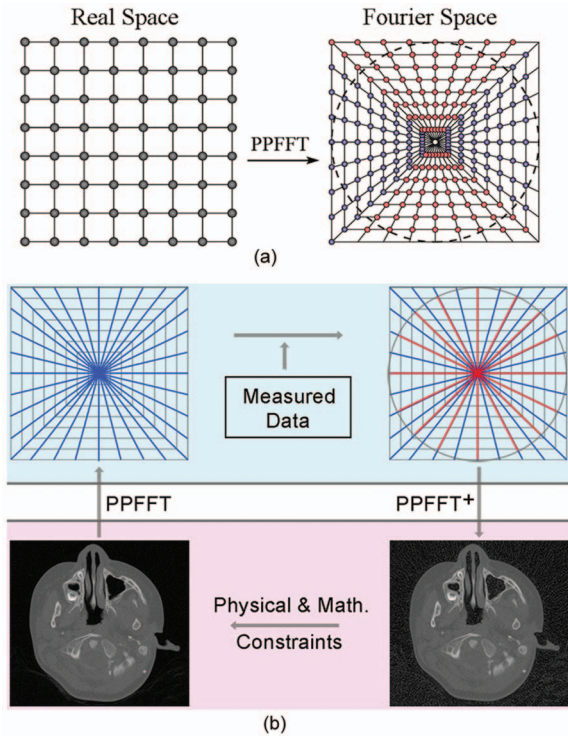


FIG. 1. (a) Geometrical representation of a Cartesian and a pseudopolar grid, related by the algebraically exact PPFFT. The dotted circle represents the resolution circle. (b) Schematic of the EST method that iterates back and forth between real and Fourier space. The forward transform from a Cartesian grid in real space (bottom-left) to a pseudopolar grid in Fourier space (top-left) is performed by the PPFFT. The inverse step from Fourier space to real space is performed by the adjoint transform of the PPFFT (PPFFT⁺). In each iteration, physical and mathematical constraints are enforced in real space (bottom-right), while measured data is applied in Fourier space. An error metric is used to monitor the convergence of the iterative algorithm.

to tomographic reconstructions. First, to accurately invert the Fourier data using the PPFFT, knowledge of $2N$ data points along the $2N$ equally sloped lines is needed.³² This requires a large number of projections and is not desirable in experiment due to radiation dose or technical restrictions. Second, the pseudopolar grid points past the resolution circle [indicated by the dotted circle in Fig. 1(a)] cannot be experimentally obtained²⁰ and thus exact reconstructions through the inverse PPFFT are not possible. Third, in order to enhance the image quality and reduce radiation dose, physical constraints and mathematical regularization have to be applied in the image reconstruction.

To overcome these difficulties, the EST method was developed, which iterates back and forth between real and Fourier space.^{20–27} The algorithm starts with padding each projection with zeros and calculating its oversampled Fourier slice in the pseudopolar grid. The oversampling concept (i.e., sampling the Fourier slice at a frequency finer than the Nyquist interval) has been widely used to solve the phase problem in coherent diffraction imaging.^{34–36} In the EST method, we implemented oversampling by padding each projection with zeros. These zeros do not provide extra information about the object but allow us to define a support in real space to facilitate the reconstruction process.

In order to transform the fan-beam projections to equally sloped lines in a pseudopolar grid, a rebinning process must be performed prior to initiating the EST iterative algorithm. We utilized the common rebinning method, implemented with two 1D interpolations.³⁷ The relation of the coordinates between a ray in the fan-beam geometry $p(\theta, \psi)$ and a ray in the parallel geometry $p(\gamma, \xi)$ is defined as⁴

$$\begin{aligned}\gamma &= \theta + \psi, \\ \psi &= \arcsin(\xi/D),\end{aligned}\quad (2)$$

where θ is the projection angle in the fan-beam geometry, ψ is the fan angle of the ray, γ is the projection angle in the parallel beam geometry, ξ is the perpendicular distance from the origin, and D is the distance from source to rotation center. The main difference with the common rebinning method is that γ is at equally sloped angular intervals. Note that, although the rebinning step requires interpolations, our numerical simulations indicate that this process does not introduce much additional noise or artifacts as long as the fan-beam projections are finely sampled. It is also important to point out that the rebinning process needs to be applied only once, prior to the initiation of the iterative process, after which point, the Fourier transform of the rebinned projections are utilized as measurement constraints. Additionally, the parallel projections are not calculated at all the $2N$ lines of the pseudopolar grid, rather only limited portion of the pseudopolar grid in Fourier space are filled with these rebinned measurement data, and the rest of the lines are filled in by the iterative algorithm as the reconstruction is solved for.

Following the above rebinning process, in the first iteration, the grid points outside the resolution circle and on the missing projections [blue lines in Fig. 1(b) top-right] are set to zero. The algorithm then iterates back and forth between real and Fourier space using the PPFFT. As shown in Fig. 1(b), the j th iteration consists of the following six steps:

- (i) Apply the adjoint of the PPFFT to the Fourier slices $F_j(k)$ and obtain a real-space image, $f_j(\vec{r})$ [Fig. 1(b) bottom-right]. Here the adjoint of the PPFFT instead of the inverse PPFFT is used because the former can significantly accelerate the convergence process without compromising the reconstruction accuracy.²³ But in the final iteration of the algorithm, the inverse PPFFT is used. The representative adjoint operation, which includes preconditioner and step size parameter for optimal performance, is implemented as detailed by Mao *et al.*²³
- (ii) Derive a new object, $f_j^r(\vec{r})$, by applying mathematical regularizations to $f_j(\vec{r})$.^{38,39} In our reconstructions, we applied the nonlocal total variation regularization (NLTV) (Ref. 40) once in every other iteration. The nonlocal total variation regularization is defined as

$$J_w(f) = \int \sqrt{\int [f(p_1) - f(p_2)]^2 w_h(p_1, p_2) dp_1 dp_2}, \quad (3)$$

where the weight function $w_h(p_1, p_2)$ describes the similarity between the patches surrounding two different pixels, p_1 and p_2 , and h is a filter parameter. The object is regularized by minimizing

$$\min_f J_w(f) + \frac{\lambda}{2} \|f - f_j\|^2, \quad (4)$$

where λ is a parameter to control the strength of TV-regularization. Smaller values of λ give stronger regularization. The regularization step is not performed in the last iteration so that the final reconstruction is consistent with the measured data. Compared to the general TV, the NLTV not only adopts the advantage of edge preserving in TV but also uses a nonlocal weighted graph to present the similarity of different pixels instead of direct subtraction, which can preserve fine structures.

- (iii) A support is determined based on the zero padding of the projections (i.e., oversampling). Outside the support, $f_j^r(\vec{r})$ is set to zero and inside the support, the negative values of $f_j^r(\vec{r})$ are set to zero as a physical constraint. A new image is obtained, defined as $f_j'(\vec{r})$ [Fig. 1(b) bottom-left].
- (iv) Apply the PPFFT to $f_j'(\vec{r})$ and obtain updated Fourier-space slices, $F_j'(\vec{k})$ [Fig. 1(b) top-left].
- (v) Obtain the Fourier slices for the $(j + 1)$ th iteration [Fig. 1(b) top-right] by replacing $F_j'(\vec{k})$ with the measured Fourier slices [red lines in Fig. 1(b)]. The grid points outside the resolution circle and on the missing Fourier slices remain unchanged.
- (vi) An error metric is calculated,

$$\text{Error} = \frac{\sum_k |F_j'(\vec{k}) - F(\vec{k})|_{k \leq R}}{\sum_k |F_j'(\vec{k}) + F(\vec{k})|_{k \leq R}}, \quad (5)$$

where $F(\vec{k})$ represents the measured Fourier slices, $F_j'(\vec{k})$ is the calculated Fourier slices in the j th iteration, and R is the radius of the resolution circle.

In general, the algorithm is stopped when the error does not decrease by more than 1% from the previous iteration. In actual experiments, it is automatically terminated when the error becomes stabilized after about 20 iterations. Relative to methods presented by Mao *et al.*,²³ the steps subsequent to the rebinning stage in the above algorithm can be regarded as a general extension of the continuation method with two distinct variations. First, instead of a TV regularization in each iteration, the NLTV is applied in every other iteration as it is found to be an experimentally effective procedure that reduces complexity while maintaining the proper effect of the regularization. Second, a fixed regularization parameter is used throughout the iterative process, as it enables for a simple and experimentally stable method.

II.C. Data acquisition

The EST method has been validated thoroughly for the parallel beam geometry in our former research work.^{20–27} In this work, the data sets were acquired from a Siemens SO-

MATOM Sensation 64 scanner under axial mode. The central slice was selected to validate the feasibility of the EST method for fan-beam geometry. A total of 1160 projections was acquired from 0° to 360° . There were 1344 detectors and the reconstruction matrix size was 1344×1344 pixels. A rebinning step was performed prior to initiating the algorithm in order to transform the fan-beam projections to parallel projections along equally sloped lines of the pseudopolar grid. Since the scanner utilizes a flying focal spot (FFS) technology to increase detector sampling, the raw projections were interlaced and corrected prior to rebinning.⁴¹

II.C.1. Phantom studies

The Siemens image quality phantom (EMMA) (Ref. 42) was used to quantify the amount of CT dose reduction achievable by the EST method. The phantom contains resolution inserts to measure the image resolution, and contrast inserts to measure the image contrast.⁴² The EMMA phantom was systematically scanned at different flux settings, ranging from a maximum of 583 mAs to a minimum of 39 mAs. All scans are performed under axial mode with the tube current modulation off and the voltage set to 120 kVp. The FBP reconstructions are performed with a standard uncropped ramp filter in conjunction with cubic interpolation for the back projection process for all doses. In the case of 39 mAs dose, the FBP reconstruction result is at last denoised by nonlocal total variation regularization (i.e., FBP + NLTV). The 39 mAs EST reconstruction was computed by using the iterative algorithm described in Sec. II.B. Both FBP + NLTV and EST used the same regularization parameter (0.0035).

II.C.2. Patient studies

To further quantify the radiation dose reduction in clinical environment with the EST method, a pediatric patient data set consisting of a cranial scan of an anonymous 8-year old boy was used. The scan was acquired under axial mode with a voltage of 120 kVp and a flux setting of 140 mAs. However, unlike the phantom studies, it is not possible to acquire repeated scans of the patient at different flux settings due to radiation dose concerns. To address this issue, we implemented an algorithm to simulate low dose patient data based on existing scans.^{43,44} Using this algorithm and the pediatric patient data set with a flux setting of 140 mAs, we generated CT scans at 39 mAs, the lowest possible flux setting of the Siemens Sensation SOMATOM 64 scanner. Both the FBP and EST reconstructions are computed in the same manner as the phantom studies.

II.D. Evaluation methods

We firstly evaluate overall image quality of the reconstruction results by observing the visibility of the fine and low contrast structures relative to the reconstruction of such objects acquired under high dose acquisition protocols that provide the benchmark image. The correlation between the

reconstructed image and the benchmark image can then be quantified by using cross-correlation. In the phantom studies, the contrast and resolution inserts are used to evaluate the image contrast and image resolution at different flux levels. In phantom studies, quantitative comparisons are done by measuring the mean values and their standard deviation at various contrast regions to calculate the SNRs and the CNRs,

$$\text{SNR} = \frac{\text{Mean}(I_{\text{ROI}})}{\text{Std}(I_{\text{ROI}})},$$

$$\text{CNR} = \frac{2 \times |\text{Mean}(I_{\text{ROI}_1}) - \text{Mean}(I_{\text{ROI}_2})|}{\text{Std}(I_{\text{ROI}_1}) + \text{Std}(I_{\text{ROI}_2})}, \quad (6)$$

where I_{ROI_1} and I_{ROI_2} represent the pixel values in the region of interest 1 and 2.

III. RESULTS

III.A. Quantification of the image contrast

The detectability of low contrast features is one of the important criteria in low dose reconstructions, especially when using iterative algorithms. We have quantified the image contrast and quality of the EST and FBP reconstructions at different flux settings by using the medium and low contrast inserts of the EMMA phantom. Figures 2(a)–2(e) show the FBP reconstructions at 583, 140, and 39 mAs, FBP + NLTV reconstruction at 39 mAs, and EST reconstruction at 39 mAs of the medium contrast insert, respectively. This insert consist of four different sets of the cylinders and the zoomed

views of the lowest contrast set of the cylinders are shown in Figs. 2(f)–2(j). The SNRs and the CNRs were also calculated for the largest diameter cylinder [indicated in Figs. 2(f)–2(j)]. Compared to the FBP and FBP + NLTV reconstructions at 140 and 39 mAs, the EST reconstruction at 39 mAs [Figs. 2(e) and 2(j)] exhibits better image quality and is almost consistent with the reference reconstruction (FBP at 583 mAs). As indicated by the arrows in the zoomed views [Figs. 2(f)–2(j)], the smallest cylinder (3 mm in diameter) in the 39 mAs EST reconstruction is as visible as that in the 583 mAs FBP reconstruction, but it almost disappears in 140 mAs FBP, 39 mAs FBP, and FBP + NLTV reconstructions. Also, the SNRs and CNRs of the 39 mAs EST reconstruction outperform all FBP, FBP + NLTV ones, including the 583 mAs reference reconstruction. However, the SNRs and CNRs have limitations and depend on the place chosen. Also, NLTV denoising could help to improve SNRs and CNRs but potentially results in patchiness phenomenon in the case of heavy noise.

Figure 3 shows the reconstruction images for the low contrast insert of EMMA phantom. Low flux results in noise which influences the image quality of the reconstructions of the low contrast insert. Figures 3(f)–3(j) show the zoomed view of the second highest contrast set of the cylinders. The second smallest cylinder (5 mm in diameter) indicated by arrows completely disappears in the 39 mAs FBP and FBP + NLTV reconstructions and is almost invisible in the 140 mAs

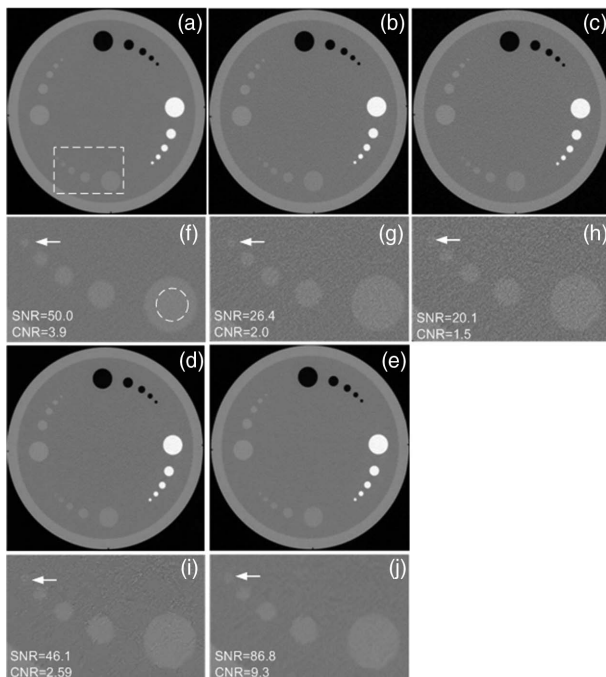


FIG. 2. Comparative reconstructions of the medium contrast insert of the EMMA phantom. Grayscale window: $[-1000, 1000]$ HU. Reconstructions of (a) 583 mAs FBP, (b) 140 mAs FBP, (c) 39 mAs FBP, (d) 39 mAs FBP + NLTV, and (e) 39 mAs EST. (g)–(j) Zoomed images of the rectangular region from (a)–(e), where the SNRs and CNRs were calculated for the largest diameter cylinder, indicated by the circle in (f).

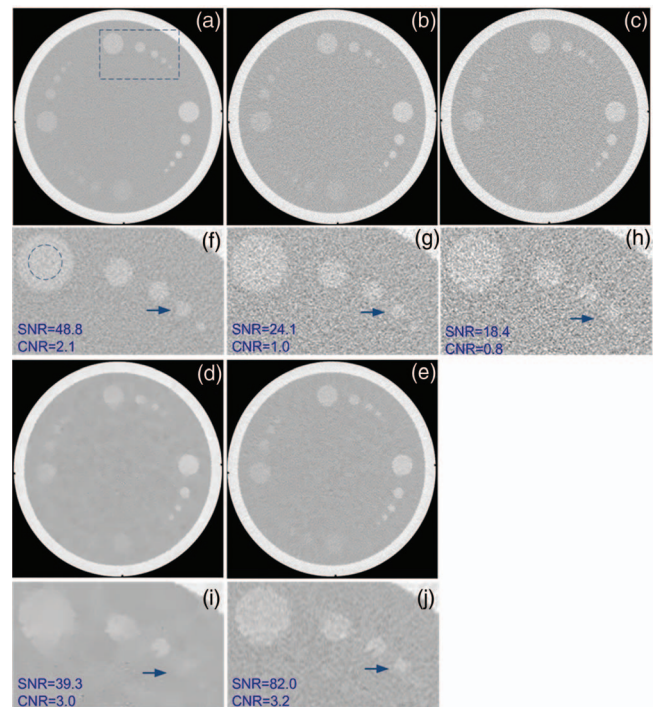


FIG. 3. Comparative reconstructions of the low-contrast insert of EMMA phantom. Gray window: $[-200, 500]$ HU (a) 583 mAs FBP, (b) 140 mAs FBP, (c) 39 mAs FBP, (d) 39 mAs FBP + NLTV, and (e) 39 mAs EST. (f)–(j) Zoomed views of the rectangular region. The 5 mm diameter cylinder is indicated by arrows. The SNRs and CNRs of the circled region, labeled in (f), were calculated for all the reconstructions.

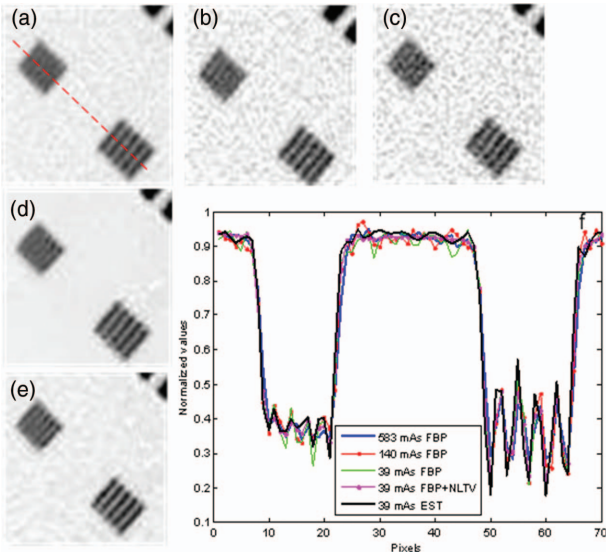


FIG. 4. Comparative reconstructions of the resolution insert of the EMMA phantom. Gray window: $[-200, 800]$ HU. Zoomed images of two smallest bar groups 10 and 11 for the reconstructions of (a) 583 mAs FBP, (b) 140 mAs FBP, (c) 39 mAs FBP, (d) 39 mAs FBP + NLTV, and (e) 39 mAs EST. (f) The line profiles along the dotted line in (a) are plotted.

FBP reconstruction, while it is still visible in the 39 mAs EST reconstruction.

III.B. Quantification of the image resolution

We quantified the image resolution of the FBP and EST reconstructions by using the resolution insert of the EMMA phantom. Figures 4(a)–4(e) show bar groups 10 and 11 in the resolution insert obtained from the 583 mAs FBP, 140 mAs FBP, 39 mAs FBP, 39 mAs FBP + NLTV, and 39 mAs EST reconstructions, respectively. The line profiles along the dotted line in Fig. 4(a) are plotted in Fig. 4(f). The smallest bar group 11 (1 line pair per mm) is not clearly discernible, but the second smallest bar group 10 (0.8 line pairs per mm) is

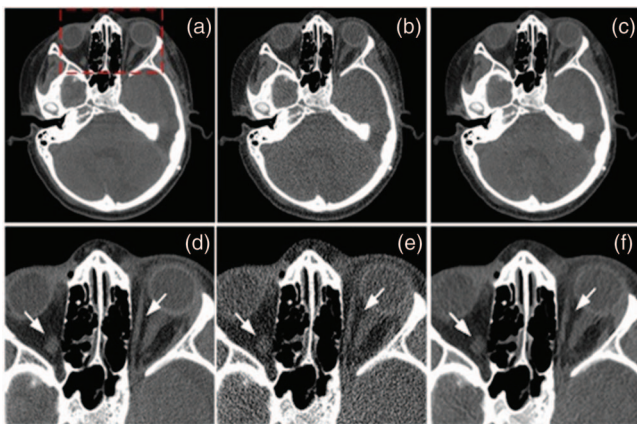


FIG. 5. Comparative reconstructions of a head slice from an anonymous pediatric patient. Gray window: $[-400, 500]$ HU. (a)–(c) Whole slice reconstructions for 140 mAs FBP, 39 mAs FBP, and 39 mAs EST. (d)–(f) The corresponding zoomed images of the rectangular region with fine and low-contrast structures. The white arrows point to some fine features.

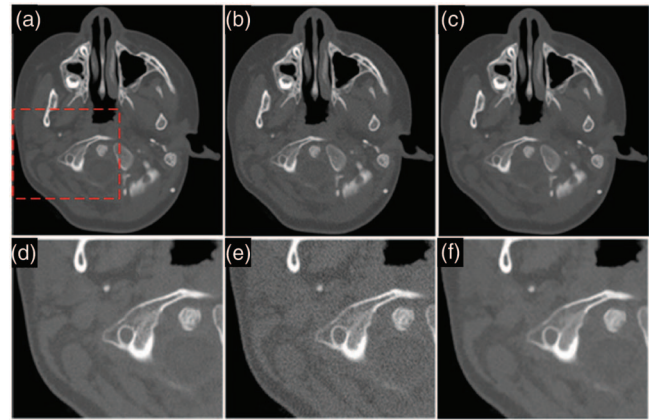


FIG. 6. Comparative reconstructions of another head slice from the same pediatric patient data set. The gray windows for (a)–(c): $[-400, 800]$ HU and for (d)–(f): $[-400, 600]$ HU. (a)–(c) Whole slice reconstructions for 140 mAs FBP, 39 mAs FBP, and 39 mAs EST. (g)–(i) The corresponding zoomed images of the rectangular region with fine and low-contrast structures.

visible in all reconstructions. In contrast to FBP reconstructions at 140 and 39 mAs, in which noise degrades the geometrical fidelity of the bars as sharp rectangular objects, the 39 mAs EST reconstruction [Fig. 4(e)] maintains a noise-free appearance similar to the 583 mAs FBP reconstruction [Fig. 4(a)].

III.C. Pediatric patient data

A total of six axial scans were acquired from the head of an anonymous pediatric patient. Figures 5 and 6 show two representative head slices reconstructed from two axial scans using 140 mAs FBP, 39 mAs FBP, and 39 mAs EST. Relative to the protocol setting of 140 mAs, the 39 mAs reconstructions simulate with 70% less imaging dose. It is noted that the SNRs of the low-dose EST reconstructions at 39 mAs are similar to SNRs of the FBP reconstructions at 140 mAs, while the image quality of the low-dose FBP reconstructions at 39 mAs are degraded by noise. The 39 mAs EST reconstruction still contains most of low-contrast structures while the 39 mAs FBP reconstruction has higher noise. Comparative reconstructions were also performed by using 140 mAs FBP, 39 mAs FBP with NLTV regularization, and 39 mAs EST with the same NLTV regularization parameters (Fig. 7). Circled regions

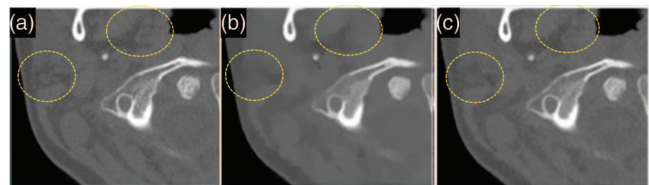


FIG. 7. Comparative reconstructions by 140 mAs FBP (a), 39 mAs FBP with NLTV regularization (b), and 39 mAs EST with the same NLTV regularization parameters (c). Circled regions indicate the degradation of fine features by simply applying the NLTV regularization to the 39 mAs FBP reconstruction. Grayscale windows: $[-400, 600]$ HU.

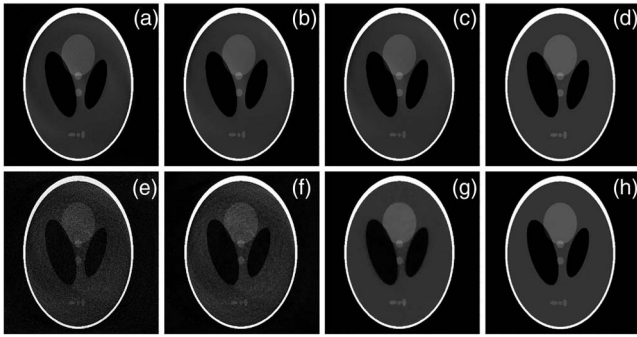


FIG. 8. Numerical experiment results on the reconstruction of the fan-beam CT data by ART, ART + TV, EM + TV, and EST. Simulation images are normalized to $[0, 1]$ with a grayscale window of $[0.01, 0.5]$. The number of projections is 360 and the number of iteration in each algorithm is 20. (a) ART; flux = 7.0×10^5 photons/pixel. (b) ART + TV; flux = 7.0×10^5 photons/pixel. (c) EM + TV; flux = 7.0×10^5 photons/pixel. (d) EST; flux = 7.0×10^5 photons/pixel. (e) ART; flux = 7.0×10^3 photons/pixel. (f) ART + TV; flux = 7.0×10^3 photons/pixel. (g) EM + TV; flux = 7.0×10^3 photons/pixel. (h) EST; flux = 7.0×10^3 photons/pixel.

indicate the degradation of fine features by simply applying the NLTV regularization to the 39 mAs FBP reconstruction.

III.D. Numerical comparisons between EST and other iterative reconstruction methods

To evaluate the reconstruction quality and computation time, we performed numerical comparisons among the EST method, the algebraic reconstruction technique (ART),^{1,2} TV-based ART (ART + TV),⁴⁵ and the TV-based expectation maximization (EM + TV) statistical reconstruction algorithm.^{46,53,54} The simulation projections were generated by a fan-beam CT scan on a 2D Shepp-Logan phantom and were added Poisson noise with a fluence of 7.0×10^5 and 7.0×10^3 photons/pixel. For a fair comparison, all iterative algorithms used the same number of iterations, the same rectangular support and the positive constraint. As Fig. 8 shows, the EST and ART + TV methods obtained comparable good-quality images with a fluence of 7.0×10^5 photons/pixel (low noise), but EST achieved better image quality than ART + TV with a fluence of 7.0×10^3 photons/pixel (high noise). Both EST and ART + TV clearly outperformed ART. The reconstructions of EM + TV and EST are comparable in both dose cases of 7.0×10^5 and 7.0×10^3 photons/pixel. The computation time of FBP, ART, ART + TV, EM + TV, and EST with a fluence of 7.0×10^3 photons/pixel is shown in Table I. Compared to ART, ART + TV and EM + TV, EST requires less than one-eighth of the computation time.

Figure 9 shows the convergence curves of the ART, ART + TV, EM + TV, and EST reconstructions with a fluence of 7.0×10^5 photons/pixel. The normalized root mean square error (RMSE) between the current and the previous iteration was calculated as a function of the number of iteration by,

$$\text{RMSE}(i-1) = \frac{\sqrt{\sum_{k=1}^n [f_{i-1}(k) - f_i(k)]^2}}{\sqrt{\sum_{k=1}^n [f_1(k) - f_2(k)]^2}}, \quad (7)$$

TABLE I. Computation time comparison for FBP, ART, ART + TV, EM + TV, and EST (number of projections: 512; detector pixels: 1024; reconstruction matrix: 512×512 pixels). The simulation parameters are based on a Siemens Sensation 64 CT scanner (source to isocenter distance: 570 mm; source to detector distance: 1060 mm; pixel width: 0.72 mm). The numerical experiment was conducted on a dual-six-core with Intel Nehalem 2.66 GHz CPUs and 4 GB Memory per core. The codes were compiled to C executable by a MATLAB compiler (mcc), and run on a Linux operating system (CentOS). For the EST reconstruction, the time for rebinning and the fractional Fourier transform before the iterative process is less than 0.5 s. The computation time for FBP is comparable with one ART iteration, including one forward and one backward projection. The extra time in FBP is due to the use of more precise cubic interpolation and the filtering process. If a simpler linear interpolation is used and the filtering step is removed, the computation time for FBP is 23.7 s.

Methods	Total time (s)	Time per iteration (s)
FBP	50.3	50.3
ART, 20 iterations	910.8	45.5
ART + TV, 20 iterations	934.2	46.7
EM + TV, 20 iterations	1449.7	72.5
EST, 20 iterations	115.38	5.8

where i is the number of iterations, $f_{i-1}(k)$ and $f_i(k)$ are the reconstructions of the i th and $(i-1)$ th iteration, k is the pixel index, and n is the amount of pixels. While all four algorithms converged after 20 iterations, EST has the fastest convergence speed.

III.E. Extending EST to helical cone-beam CT

Modern CT scanners use the axial and helical cone-beam geometry because they can significantly increase the image acquisition speed relative to the fan-beam geometry. The cone-beam geometry requires more sophisticated reconstruction methods.¹⁻⁴ Currently, the FDK method is one of the popular cone-beam reconstruction techniques.¹⁸ In this section,

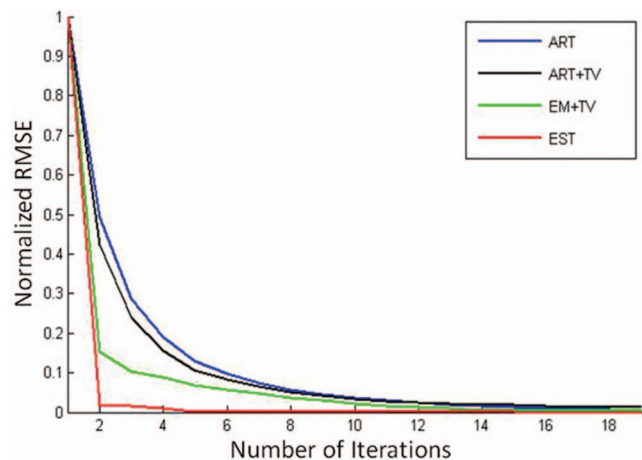


FIG. 9. Convergence curves for the ART, ART + TV, EM + TV, and EST reconstructions showing the normalized root mean square error (RMSE) as a function of the number of iterations. The fast convergence of the EST reconstruction is due to the use of the adjoint of the PPFPT instead of the inverse PPFPT (Ref. 23).

TABLE II. Simulation parameters used for the reconstruction of the helical cone-beam CT data. The geometrical parameters are similar to those in Ref. 52 and the dimensions of the 3D Shepp-Logan phantom are 138, 184, and 180 mm along the x , y , and z -axis, respectively. The size of reconstructed images is $512 \times 512 \times 512$ voxels.

Detector type	Cylindrical
Detector row	64
Detector column	512
Pixel width	0.78 mm
Pixel height	0.78 mm
Distance from the source to the detector	1005 mm
Distance from the source to the center	570 mm
The helical pitch	0.8
Total projections in each circle	720

we extend EST to the helical cone-beam geometry and compare it with FDK by using a numerical experiment.

For helical cone-beam CT, several rebinning methods have been developed.^{47–51} Among them, the Advanced Single-Slice Rebinning (ASSR) method⁴⁹ is an effective algorithm

which uses virtual tilted reconstruction planes along a helical path to Z-interpolate the images onto a Cartesian grid. The key step in ASSR is to rebin the helical cone-beam data into a series of 2D projections along virtual tilted planes that can be reconstructed by using conventional 2D FBP.

In our approach, we first used ASSR to rebin the helical cone-beam projections into a series of tilted slices along a helical path. Each tilt slice was reconstructed by EST and the series of 2D reconstructions was then interpolated along the z axis to obtain a 3D image. After implementing EST in the helical cone-beam geometry, we performed a numerical experiment on a 3D Shepp-Logan phantom. Table II shows the parameters used to generate the helical cone-beam CT data. Poisson noise was added to the helical cone-beam projections with a fluence of 7.0×10^3 photons/pixel. In the numerical experiment, we computed the reconstructions of the 3D Shepp-Logan phantom by using FDK,¹⁸ conventional ASSR,⁴⁹ and EST with ASSR. Figures 10(a)–10(i) show three different horizontal slices ($Z = -30, 0,$ and 23 mm) reconstructed by FDK, ASSR, and EST with ASSR. Quantitatively, the horizontal and vertical line scans, shown in Figs. 10(j) and 10(k), indicate that EST with ASSR produced a 3D reconstruction with highest image fidelity and least noise among the three reconstruction methods. Although the combination of EST and ASSR works well for simulated helical cone beam CT data, the extension of EST to circular cone beam CT data has not been demonstrated and will be pursued in follow-up studies.

IV. DISCUSSION AND CONCLUSION

There is no single metric that can adequately quantify image quality, and in the analysis of image quality and aggregate of metrics, both subjective and objective, must be considered along with purpose of the imaging task. The purpose of this paper is to address the feasibility of performing low dose reconstructions using an efficient Fourier based algorithm and regularization method. Due to the complexity of the analysis of image quality, in general, one cannot readily derive a specific dose reduction factor in simplistic terms. However, the results in this work demonstrate an enhanced performance of the proposed algorithm, relative to the conventional method, in the realm of low dose fan-beam CT. The evaluation utilized is firstly a comparison to a high dose reconstruction. Accordingly, for the image quality phantom analysis, data sets, acquisitions, and reconstructions were made the highest possible flux setting of the scanner at 583 mAs, protocol setting of 140 mAs, followed by EST reconstructions of 39 mAs which deliver 70% lower dose than the protocol 140 mAs. Although equivalence cannot be claimed in such low dose reconstructions due to the complexity of image analysis, it is demonstrated that in both the EMMA imaging quality phantom and a pediatric patient data acquired from a clinical CT scanner, that the 39 mAs EST reconstruction produces comparable image quality, resolution and contrast relative to 140 mAs FBP reconstruction.

The proposed EST method also provides an efficient way to enforce measured data in Fourier space, which through the PPFIT constitutes an accurate and fast method for

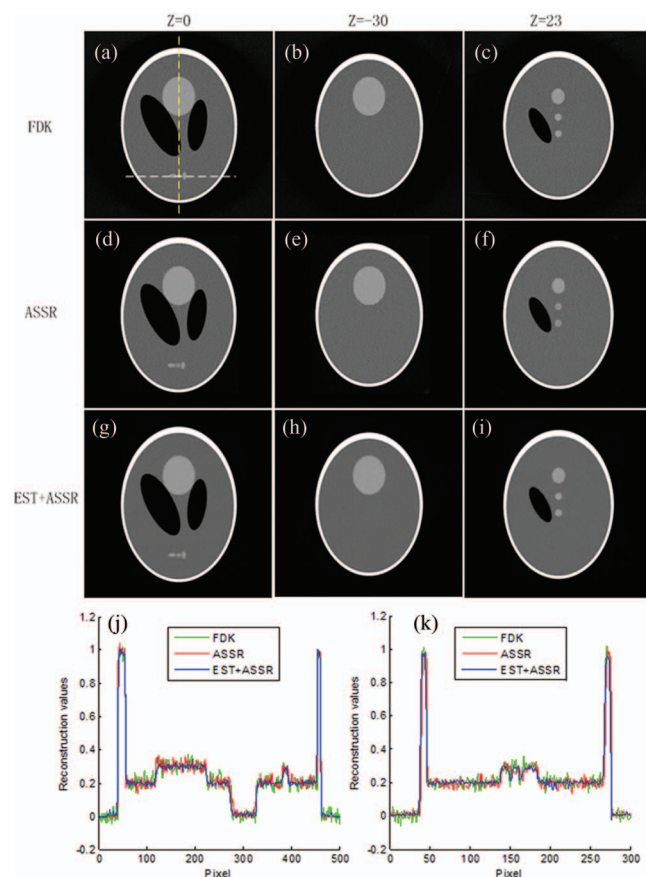


FIG. 10. Numerical experiment on the reconstruction of helical cone-beam CT data by FDK, conventional ASSR, and EST with ASSR. (a)–(c) Three representative slices of the FDK reconstruction with $Z = -30, 0,$ and 23 mm. The grayscale window of the images is $[0.01, 0.5]$. (d)–(f) The same three slices reconstructed by the conventional ASSR method with 2D FBP and TV regularization. (g)–(i) The same three slices reconstructed by EST with ASSR and TV regularization. (j) Line scan along the yellow line for (a), (d), and (g). (k) Line scan along the white line for (a), (d), and (g).

calculating the equivalent of forward and back projections. This allows any regularization constraint to be implemented in manner such that the final reconstruction result is consistent with the measured data, since in each iteration, including the final step of the iterative algorithm, the measured data is reinforced in Fourier space. This is to be contrasted by a method that simply applies denoising or regularization to FBP reconstructions, as by doing so, there is no guarantee that the final image is consistent with patient measurements, or that over-smoothing and loss of important features have not occurred. To demonstrate this more thoroughly, the NLTV regularization was simply applied to the FBP reconstructions in both the phantom and patient data. As expected, the high contrast resolution is not considerably affected by such a procedure; however, the fine contrast features such as those shown Figs. 5 and 6 by the arrows are degraded. Figure 7 shows a comparison of regions for the pediatric patient data using NLTV with the exact same parameters as the EST algorithm, which demonstrate that some structures (shown in dashed circles) are lost if such a simple method is attempted.

Numerical comparisons between EST and other iterative methods were also conducted. While both the EST method and the EM statistical algorithm produced good quality reconstructions, EST required much less computation time than EM. It is also important to note that the EM statistical algorithm used here has been developed for emission tomography, and may not represent the ideal case for x-ray CT data. As more advanced statistical algorithms have been developing (see, e.g., Ref. 13), further studies are needed to fully evaluate the potential and limit of the EST method relative to these statistical algorithms. Furthermore, since there is a rebinning step before initializing the iterative process, compared to non-rebinning reconstruction algorithms, the error comes from rebinning might increase for EST when there are fewer number of measured projections. Finally, the extension of EST to helical cone beam CT data has been explored. Our numerical experiment suggests that the combination of EST with ASSR can achieve better reconstructions of helical cone beam data than the FDK and conventional ASSR methods in terms of image fidelity and noise level.

ACKNOWLEDGMENTS

The authors thank Henry Huang and Hui Xue for stimulating discussion. This work was partially supported by UC Discovery/TomoSoft Technologies grant IT107-10166. Stanley Osher was supported by National Science Foundation (NSF) grants DMS0835863 and DMS0914561.

^{a)}Electronic mail: miao@physics.ucla.edu

¹A. C. Kak and M. Slaney, *Principles of Computerized Tomographic Imaging* (SIAM, Philadelphia, 2001).

²G. T. Herman, *Fundamentals of Computerized Tomography: Image reconstruction from projection*, 2nd ed. (Springer, New York, 2009).

³J. Hsieh, *Computed Tomography: Principles, Design, Artifacts, and Recent Advances*, 2nd ed. (Wiley, Washington, 2009).

⁴T. M. Buzug, *Computed Tomography: From Photons Statistics to Modern Cone-Beam CT* (Springer, Berlin, 2008).

- ⁵A. Berrington de Gonzalez *et al.*, "Projected cancer risks from computed tomographic scans performed in the United States in 2007," *Arch. Intern. Med.* **169**, 2071–2077 (2009).
- ⁶R. Smith-Bindman *et al.*, "Radiation dose associated with common computed tomography examinations and the associated lifetime attributable risk of cancer," *Arch. Intern. Med.* **169**, 2078–2086 (2009).
- ⁷R. H. Fazel *et al.*, "Exposure to low-dose ionizing radiation from medical imaging procedures," *N. Engl. J. Med.* **361**, 849–857 (2009).
- ⁸A. J. Einstein *et al.*, "Radiation dose and cancer risk estimates in 16-slice computed tomography coronary angiography," *J. Nucl. Cardiol.* **15**, 232–240 (2008).
- ⁹S. Kim, T. Yoshizumi, D. P. Frush, G. Toncheva, and F. F. Yin, "Radiation dose from cone beam CT in a pediatric phantom: Risk estimation of cancer incidence," *AJR, Am. J. Roentgenol.* **194**, 186–190 (2010).
- ¹⁰NCRP Report No. 160, Ionizing Radiation Exposure of the Population of the United States, National Council on Radiation Protection and Measurements, 2009.
- ¹¹E. Candes, J. Romberg, and T. Tao, "Exact signal reconstruction from highly incomplete frequency information," *IEEE Trans. Inf. Theory* **52**, 489–509 (2006).
- ¹²G. H. Chen, J. Tang, and S. Leng, "Prior image constrained compressed sensing (PICCS): A method to accurately reconstruct dynamic CT images from highly undersampled projection data sets," *Med. Phys.* **35**(2), 660–663 (2008).
- ¹³E. Y. Sidky and X. Pan, "Image reconstruction in circular cone-beam computed tomography by constrained, total-variation minimization," *Phys. Med. Biol.* **53**(17), 4777–4807 (2008).
- ¹⁴H. Yu and G. Wang, "Compressed sensing based interior tomography," *Phys. Med. Biol.* **54**(9), 2791–2805 (2009).
- ¹⁵G. H. Chen *et al.*, "Temporal resolution improvement using PICCS in MDCT cardiac imaging," *Med. Phys.* **36**(6), 2130–2135 (2009).
- ¹⁶J. C. Ramirez-Giraldo *et al.*, "Nonconvex prior image constrained compressed sensing (NCPICCS): Theory and simulations on perfusion CT," *Med. Phys.* **38**(4), 2157–2167 (2011).
- ¹⁷L. Ritschl *et al.*, "Improved total variation-based CT image reconstruction applied to clinical data," *Phys. Med. Biol.* **56**(6), 1545–1561 (2011).
- ¹⁸H. Kudo and T. Saito, "Helical-scan computed tomography using cone-beam projections," in *IEEE Nuclear Science Symposium and Medical Imaging Conference, Santa Fe, New Mexico* (IEEE, 1991), pp. 1958–1962.
- ¹⁹X. Pan, E. Y. Sidky, and M. Vannier, "Why do commercial CT scanners still employ traditional, filtered back-projection for image reconstruction?" *Inverse Probl.* **25**, 123009 (2009).
- ²⁰J. Miao, F. Förster, and O. Levi, "Equally sloped tomography with over-sampling reconstruction," *Phys. Rev. B* **72**, 052103 (2005).
- ²¹J. Miao, C. C. Chen, C. Song, Y. Nishino, Y. Kohmura, T. Ishikawa, D. Ramunno-Johnson, T. K. Lee, and S. H. Risbud, "Three-dimensional GaN-Ga₂O₃ core shell structure revealed by x-ray diffraction microscopy," *Phys. Rev. Lett.* **97**, 215503 (2006).
- ²²E. Lee, B. P. Fahimian, C. V. Iancu, C. Suloway, G. E. Murphy, E. R. Wright, D. Castaño-Díez, G. J. Jensen, and J. Miao, "Radiation dose reduction and image enhancement in biological imaging through equally-sloped tomography," *J. Struct. Biol.* **164**(2), 221–227 (2008).
- ²³Y. Mao, B. P. Fahimian, S. Osher, and J. Miao, "Development and optimization of regularized tomographic reconstruction algorithms utilizing equally-sloped tomography," *IEEE Trans. Image Process.* **19**(5), 1259–1268 (2010).
- ²⁴B. P. Fahimian, Y. Mao, P. Cloetens, and J. Miao, "Low dose x-ray phase-contrast and absorption CT using equally-sloped tomography," *Phys. Med. Biol.* **55**, 5383–5400 (2010).
- ²⁵H. Jiang, C. Song, C.-C. Chen, R. Xu, K. S. Raines, B. P. Fahimian, C. Lu, T.-H. Lee, A. Nakashima, J. Urano, T. Ishikawa, F. Tamanoi, and J. Miao, "Quantitative 3D imaging of whole, unstained cells by using x-ray diffraction microscopy," *Proc. Natl. Acad. Sci. U.S.A.* **107**, 11234–11239 (2010).
- ²⁶M. C. Scott, C.-C. Chen, M. Mecklenburg, C. Zhu, R. Xu, P. Ercius, U. Dahmen, B. C. Regan, and J. Miao, "Electron tomography at 2.4 Å resolution," *Nature (London)* **483**, 444–447 (2012).
- ²⁷Y. Zhao, E. Brun, P. Coan, Z. Huang, A. Sztróky, P. C. Diemoz, S. Lieberhardt, A. Mittone, S. Gasilov, J. Miao, and A. Bravin, "High resolution, low dose phase contrast x-ray tomography for 3D diagnosis of human breast cancers," *Proc. Natl. Acad. Sci. U.S.A.* **109**, 18290–18294 (2012).
- ²⁸S. Matej, J. A. Fessler, and I. G. Kazantsev, "Iterative tomographic image reconstruction using Fourier-based forward and back-projectors," *IEEE Trans. Med. Imaging* **23**, 401–412 (2004).

- ²⁹Y. Zhang-O'Connor and J. A. Fessler, "Fourier-based forward and back-projectors in iterative fan-beam tomographic image reconstruction," *IEEE Trans. Med. Imag.* **25**, 582–589 (2006).
- ³⁰W. L. Briggs and V. E. Henson, *The DFT: An Owner's Manual for the Discrete Fourier Transform*, 3rd ed. (SIAM, Philadelphia, 1995).
- ³¹R. M. Mersereau and A. V. Oppenheim, "Digital reconstruction of multidimensional signals from their projections," *Proc. IEEE* **62**, 1319–1338 (1974).
- ³²A. Averbuch *et al.*, "A framework for discrete integral transformations I—The pseudopolar Fourier transform," *SIAM J. Sci. Comput. (USA)* **30**(2), 785–803 (2008).
- ³³D. H. Bailey and P. N. Swartztrauber, "The fractional Fourier transform and applications," *SIAM Rev.* **33**(3), 389–404 (1991).
- ³⁴J. Miao, P. Charalambous, J. Kirz, and D. Sayre, "Extending the methodology of X-ray crystallography to allow imaging of micrometre-sized non-crystalline specimens," *Nature (London)* **400**, 342–344 (1999).
- ³⁵J. Miao, T. Ishikawa, T. Earnest, and Q. Shen, "Extending the methodology of x-ray crystallography to allow structure determination of non-crystalline materials, whole cells and single macromolecular complexes," *Annu. Rev. Phys. Chem.* **59**, 387–409 (2008).
- ³⁶K. S. Raines, S. Salha, R. L. Sandberg, H. Jiang, J. A. Rodríguez, B. P. Fahimian, H. C. Kapteyn, J. Du, and J. Miao, "Three-dimensional structure determination from a single view," *Nature (London)* **463**, 214–217 (2010).
- ³⁷A. H. Delaney and Y. Bresler, "A fast and accurate Fourier algorithm for iterative parallel-beam tomography," *IEEE Trans. Image Process.* **5**(5), 740–753 (1996).
- ³⁸S. Osher, M. Burger, D. Goldfarb, J. Xu, and W. Yin, "An iterative regularization method for total variation-based image restoration," *Multiscale Model. Simul.* **4**, 460–489 (2005).
- ³⁹A. Buades, B. Coll, and J. M. Morel, "A review of image denoising algorithms, with a new one," *Multiscale Model. Simul.* **4**, 490–530 (2005).
- ⁴⁰G. Gilboa and S. Osher, "Nonlocal operators with applications to image processing," *Multiscale Model. Simul.* **7**, 1005–1028 (2008).
- ⁴¹Y. Kyriakou, M. Kachelriess, M. Knaup, J. U. Krause, and W. A. Kalender, "Impact of the z-flying focal spot on resolution and artifact behavior for a 64-slice spiral CT scanner," *Eur. Radiol.* **16**(6), 1206–1215 (2006).
- ⁴²O. Gayou and M. Miften, "Commissioning and clinical implementation of a megavoltage cone beam CT system for treatment localization," *Med. Phys.* **34**, 3183–3192 (2007).
- ⁴³P. Massoumzadeh *et al.*, "Validation of CT dose-reduction simulation," *Med. Phys.* **36**(1), 174–189 (2009).
- ⁴⁴B. R. Whiting *et al.*, "Properties of preprocessed sinogram data in x-ray computed tomography," *Med. Phys.* **33**(9), 3290–3303 (2006).
- ⁴⁵E. Sidky, C. M. Kao, and X. Pan, "Accurate image reconstruction from few-views and limited-angle data in divergent-beam CT," *J. X-Ray Sci. Technol.* **14**, 119–139 (2006).
- ⁴⁶L. Shepp and Y. Vardi, "Maximum likelihood reconstruction for emission tomography," *IEEE Trans. Med. Imaging* **1**, 113–122 (1982).
- ⁴⁷F. Noo, M. Defrise, and R. Clackdoyle, "Single-slice rebinning method for helical cone-beam CT," *Phys. Med. Biol.* **44**(2), 561–570 (1999).
- ⁴⁸J. Hsieh and X. Tang, "Tilted cone-beam reconstruction with row-wise fan-to-parallel rebinning," *Phys. Med. Biol.* **51**(20), 5259–5276 (2006).
- ⁴⁹M. Kachelriess, S. Schaller, and W. A. Kalender, "Advanced single-slice rebinning in cone-beam spiral CT," *Med. Phys.* **27**(4), 754–772 (2000).
- ⁵⁰S. Schaller *et al.*, "New, efficient Fourier-reconstruction method for approximate image reconstruction in spiral cone-beam CT at small cone angles," *Proc. SPIE* **3032**, 213–224 (1997).
- ⁵¹M. Defrise, F. Noo, and H. Kudo, "Rebinning-based algorithms for helical cone-beam CT," *Phys. Med. Biol.* **46**, 2911–2937 (2001).
- ⁵²Y. Zou and X. Pan, "Exact image reconstruction on PI-lines from minimum data in helical cone-beam CT," *Phys. Med. Biol.* **49**, 941–959 (2004).
- ⁵³K. Lange and R. Carson, "EM reconstruction algorithms for emission and transmission tomography," *J. Comput. Assist. Tomogr.* **8**(2), 302–316 (1984).
- ⁵⁴M. Yan and L. Vese, "Expectation maximization and total variation based model for computed tomography reconstruction from undersampled data," *Proc. SPIE* **7961**, 79612X (2011).